

Canonical Variates in Wasserstein Metric Space

Jia Li

Department of Statistics, The Pennsylvania State University

Lin Lin

Department of Biostatistics and Bioinformatics, Duke University

Abstract

In this paper, we address the classification of instances each characterized not by a singular point, but by a distribution on a vector space. We employ the Wasserstein metric to measure distances between distributions, which are then used by distance-based classification algorithms such as k-nearest neighbors, k-means, and pseudo-mixture modeling. Central to our investigation is dimension reduction within the Wasserstein metric space to enhance classification accuracy. We introduce a novel approach grounded in the principle of maximizing Fisher’s ratio, defined as the quotient of between-class variation to within-class variation. The directions in which this ratio is maximized are termed discriminant coordinates or canonical variates axes. In practice, we define both between-class and within-class variations as the average squared distances between pairs of instances, with the pairs either belonging to the same class or to different classes. This ratio optimization is achieved through an iterative algorithm, which alternates between optimal transport and maximization steps within the vector space. We conduct empirical studies to assess the algorithm’s convergence and, through experimental validation, demonstrate that our dimension reduction technique substantially enhances classification performance. Moreover, our method outperforms well-established algorithms that operate on vector representations derived from distributional data. It also exhibits robustness against variations in the distributional representations of data clouds.

Keywords: Optimal transport, Wasserstein distance, Canonical coordinates, Dimension reduction, Classification, Distributional data

1 Introduction

In numerous biomedical contexts, a prevalent challenge is the classification of subjects, each represented as what is termed a ‘data cloud’. A prime example is cellular-based immuno-

profiling, a technique extensively employed to monitor immune responses in individuals in response to various stimuli, including disease, therapeutic interventions, and vaccinations. Widely adopted single-cell technologies, such as flow cytometry, mass cytometry (CyTOF), and single-cell RNA sequencing (scRNA-seq), facilitate the measurement of cellular constituents from a sample (often blood) of an individual (Furman et al., 2013; Lin et al., 2015; Lingblom et al., 2018; Aleman et al., 2021; Stefanski et al., 2022; Zhang et al., 2023; Rubio et al., 2023). The resultant single-cell data are organized into a matrix format, with each row depicting a measured cell and each column representing specific cell markers (such as proteins or genes) for a sample. This matrix is important in predicting outcomes or disease status in individual subjects. However, this matrix form, in contrast to traditional vector or tabular data, embodies a unique characteristic: each instance is a matrix, with each row constituting a distinct point (cell) within the single-cell data cloud. A crucial aspect to recognize here is the distinction between a standard matrix and a 'data-cloud matrix'. In the latter, the sequential order of rows is non-informative. Consequently, random shuffling of rows does not affect the intrinsic characteristics of the data cloud in any way.

In this paper, we conceptualize a data cloud as a specific form of a distribution, wherein the data points are considered as support points of a uniform distribution. If these points are assigned unequal weights, the set can still be regarded as a distribution albeit non-uniform. For continuous distributions, we focus on the highly representative *Gaussian Mixture Model* (GMM). While classification or clustering methods tailored for distributional data are often employed in the analysis of data clouds, these techniques also have broader applications, such as in model integration.

There are two major schools of approaches to the classification of data clouds. In the first school, data clouds are transformed to feature vectors via clustering. In scenarios where clusters, generated for different instances, are assigned coherent labels, attributes of each cluster (such as cluster proportion and mean values) can be aggregated into a feature vector. This transformation from data clouds to vectors is advantageous, as it enables the application of a broad spectrum of machine learning algorithms. Often, coherent cluster labels are derived from supplementary information or ensured by manual inspection.

Nonetheless, a challenge arises when algorithm-generated clusters do not naturally align to produce coherent labels, thereby complicating the creation of vector representations. The limitations of this vector representation approach will be discussed in more detail subsequently. In the second school of approaches, data clouds are represented as distributions, which are then processed using classification algorithms specifically designed for distributional data. Given the lack of algebraic structure at the instance level in distributional data, this approach predominantly relies on distance-based classification algorithms. A frequently employed measure in this context is the Wasserstein metric.

In the context of single-cell data analysis, as exemplified earlier, the traditional methodology typically involves the initial identification of cell subsets within the single-cell dataset. This identification is achieved either through a clustering algorithm or a manual gating strategy (Brummelman et al., 2019). Following this, summary statistics of these identified cell subsets, such as the proportion and mean marker expression levels, are compiled into a vector to facilitate outcome prediction. However, while the use of summary statistics as features offers a convenient route for prediction, this approach harbors a significant limitation: it often neglects various distributional characteristics among cells. These characteristics, including multi-modality, skewness, and variance, can be crucial in conveying important information. The concept of representing single-cell data (or data cloud) as a distribution has been gaining traction, particularly in the analysis of scRNA-seq for *differential expression* (DE) analysis (Korthauer et al., 2016; Zhang et al., 2022; Zhang and Guo, 2022). In this approach, a distribution is typically derived from a single marker or feature. For datasets with multiple measured features, a one-dimensional distribution is fitted for each feature, and the DE analysis is then conducted independently for each feature.

In this paper, we focus on the second approach to the classification of distributional data. A fundamental question we address is the principled reduction of dimensionality in the context of distance-based classification, particularly when employing the Wasserstein metric. As detailed in the subsequent section, we explore the application of maximizing Fisher’s ratio within the Wasserstein metric space. Due to the inherent link between variance and the sum of all pairwise Euclidean distances, Fisher’s ratio can be defined using

only pairwise distances. We adopt the definition based on pairwise distances. This perspective naturally suggests alternatives to the standard definition of Fisher’s ratio. Specifically, in our study, we explore a scheme of only considering pairwise distances between instances that are potentially difficult to classify. This strategy often yields better classification after dimension reduction.

To tackle the computational intensiveness of the Wasserstein distance, an approximation called the sliced-Wasserstein distance (Bonneel et al., 2015) is proposed, based on linear slicing of probabilistic distributions. Further extensions such as the max-sliced-Wasserstein (Deshpande et al., 2019; Paty and Cuturi, 2019) and generalized sliced Wasserstein (Kolouri et al., 2019) have been explored. Although a linear projection or subspace is searched to compute the max-sliced-Wasserstein, the objective is different from our aim of maximizing Fisher’s ratio.

It is worthwhile to note an interesting method called Wasserstein discriminant analysis (WDA) by Flamary et al. (2018) for data in the Euclidean space. Although our work also involves the Wasserstein distance, the research problem addressed here is intrinsically different than that of WDA. In Flamary et al. (2018), a new criterion is developed for discriminant analysis on data points in the Euclidean space; and the Wasserstein metric is used to measure the distance between class-level distributions. In contrast, our work aims at dimension reduction for data instances that are distributions themselves. At the class level, instead of using the Wasserstein distance, we opt for a simple summation of pairwise distances, as has been adopted in Fisher’s ratio or other related criteria. Our novelty does not stem from introducing a new optimization criterion for vector data, but rather from addressing the complexities inherent in handling a more challenging data type, i.e., discrete or continuous distributions.

For continuous distributions, our solution involves adopting the Gaussian Mixture Model (GMM) as a versatile mechanism for representation. We further propose substituting the Wasserstein metric with the Minimized Aggregated Wasserstein (MAW) distance (Chen et al., 2019). This substitution facilitates the development of an efficient optimization algorithm. A discrete distribution with finite support can be viewed as a finite GMM with

singular covariance matrices (i.e., zero variances in all dimensions), and the MAW distance simplifies to the standard Wasserstein distance in this case. Therefore, our method derived for the MAW distance applies seamlessly to discrete distributions. Discretization (or sampling) and modeling by GMM are two major approaches for approximating continuous distributions. Our method is applicable to either form of approximation.

The rest of the paper is organized as follows. Section 2 details the formulation of the dimension reduction problem and the corresponding optimization algorithm. Experimental results are provided in Section 3. We conclude in Section 4.

2 Algorithm

2.1 Optimization criterion

Consider a collection of distributions \mathcal{Q}_k , $k = 1, \dots, n$, where n is the sample size, i.e., the number of distributions. We first consider discrete distribution $\mathcal{Q}_k = \{(p_j^{(k)}, x_j^{(k)}), j = 1, \dots, m_k\}$, where m_k is the number of support points, $p_j^{(k)}$ is the probability on the j th support point $x_j^{(k)}$ ($x_j^{(k)} \in \mathbb{R}^d$, the d -dimensional Euclidean space) of the k th distribution. In practice, we often use the empirical distribution of a dataset, which is a discrete uniform distribution on the data points. Extension to GMM will be discussed later. Denote the class label associated with \mathcal{Q}_k by Y_k , $Y_k \in \mathcal{Y}$, $\mathcal{Y} = \{1, \dots, M\}$, where M is the number of classes.

Define a *coupling* Π^* of the two distributions \mathcal{Q}_{k_1} and \mathcal{Q}_{k_2} as a distribution over the Cartesian product $(x_i^{(k_1)}, x_j^{(k_2)})$ such that $\sum_{j=1}^{m_{k_2}} \pi_{i,j} = p_i^{(k_1)}$, $i = 1, \dots, k_1$ and $\sum_{i=1}^{m_{k_1}} \pi_{i,j} = p_j^{(k_2)}$, $j = 1, \dots, k_2$. These constraints on $\pi_{i,j}$'s are called the *marginal constraints* in *optimal transport* (OT) (Villani, 2003). Let Π_{k_1, k_2} be the set of all couplings. The L_2 norm Wasserstein distance between \mathcal{Q}_{k_1} and \mathcal{Q}_{k_2} is defined as follows, which is essentially an OT problem.

$$W^2(\mathcal{Q}_{k_1}, \mathcal{Q}_{k_2}) = \min_{\pi \in \Pi_{k_1, k_2}} \sum_{i=1}^{m_{k_1}} \sum_{j=1}^{m_{k_2}} \pi_{i,j} \|x_i^{(k_1)} - x_j^{(k_2)}\|^2. \quad (1)$$

Let $a_i = (a_{1,i}, a_{2,i}, \dots, a_{d,i})^t \in \mathbb{R}^d$ be a projection direction (not normalized). Let $A =$

$(a_1, a_2, \dots, a_{d'})$ be a matrix of dimension $d \times d'$, where $d' < d$. The linear transform to reduce the dimension of $x \in \mathbb{R}^d$ to d' is $A^t \cdot x$. We call the distribution induced by the projection of the support points to the lower dimension the *projected distribution* and denote it by $P(\mathcal{Q}_k, A) = \{(p_j^{(k)}, A^t \cdot x_j^{(k)}), j = 1, \dots, m_k\}$. With a slight abuse of notation, for vector $a \in \mathbb{R}^d$, $P(\mathcal{Q}_k, a) = \{(p_j^{(k)}, a^t \cdot x_j^{(k)}), j = 1, \dots, m_k\}$.

Let set \mathcal{I}_B contain pairs of indices (k_1, k_2) such that the k_1 th and k_2 th instances have different classes, that is, $Y_{k_1} \neq Y_{k_2}$. Let \mathcal{I}_W contain pairs of indices belonging to the same class. As will be discussed later, \mathcal{I}_B (or \mathcal{I}_W) may not contain all the pairs of instances with different classes (or all the pairs within the same class). Define the average between-class variation by

$$\bar{V}_B(A) = \frac{1}{|\mathcal{I}_B|} \cdot \sum_{(k_1, k_2) \in \mathcal{I}_B} W^2(P(\mathcal{Q}_{k_1}, A), P(\mathcal{Q}_{k_2}, A)), \quad (2)$$

and the within-class variation by

$$\bar{V}_W(A) = \frac{1}{|\mathcal{I}_W|} \cdot \sum_{(k_1, k_2) \in \mathcal{I}_W} W^2(P(\mathcal{Q}_{k_1}, A), P(\mathcal{Q}_{k_2}, A)). \quad (3)$$

Finally, define *Fisher's ratio of variations*:

$$r(A) = \frac{\bar{V}_B(A)}{\bar{V}_W(A)}. \quad (4)$$

Again, with a slight abuse of notation, if we consider projection on one direction $a \in \mathbb{R}^d$, we use notations $\bar{V}_B(a)$, $\bar{V}_W(a)$, and $r(a)$.

The *Fisher's optimization criterion* to find an optimal projection direction is to maximize Fisher's ratio $r(a)$:

$$r(a^*) = \arg \max_a r(a). \quad (5)$$

We provide a few remarks on the Fisher's ratio and Fisher's optimization criterion. First, the concepts of Fisher's ratio and Fisher's optimization criterion were originally formulated in the context of linear discriminant analysis (LDA) (Hastie et al., 2009). We utilize these terms in our work, as the underlying principle remains consistent, namely, the maximization of the ratio between between-class and within-class variation. Within the realm of LDA, Fisher's ratio is also referred to as the *Rayleigh-Ritz quotient*.

Second, in the classical definition of Fisher’s ratio, the between-class variation is determined by the variance of the projected mean vectors for each class, with weighting according to class proportions. Similarly, the within-class variation is defined as the weighted average of variances for each projected class. In the computation of these variances within the framework of LDA, per-class means are calculated as the arithmetic means of vectors. On the other hand, it can be shown that in the Euclidean space, the sample variance can be computed from the sample mean of pairwise squared distances, the two differing only by a constant factor. However, in the Wasserstein metric space, the equivalent of the arithmetic mean is the Wasserstein barycenter, whose computation is notably more demanding. By adopting the definition of Fisher’s ratio based on pairwise distances, we avoid the need of computing barycenters. Nevertheless, efficient algorithms for computing Wasserstein barycenters have been developed by Benamou et al. (2015); Ye et al. (2017); Yang et al. (2021). A key rationale for using pairwise distances is that this approach provides the flexibility of selecting pairwise distances for computing Fisher’s ratio. Empirical evidence suggests that prioritizing pairs more likely to contribute to classification errors often leads to enhancements in classification accuracy.

Finally, in the framework of LDA, the maximization of Fisher’s ratio is achieved through eigenvalue decomposition, as detailed in (Hastie et al., 2009). However, the optimization problem as outlined in Equation (5) presents unique challenges when applied to the Wasserstein distance. This complexity arises because the Wasserstein distance cannot be computed using a closed-form expression; instead, it necessitates numerical optimization. To address this, our primary strategy involves partitioning the variables involved in the optimization process into two distinct groups: the coupling weights used in calculating the Wasserstein distances, and the projection direction vector a . We then iteratively update these groups of variables in an alternating fashion.

We propose an iterative algorithm, referred to as *Optimal Transport And Fisher’s optimization* (OTAF), to solve the optimal projection direction a^* . The algorithm essentially performs coordinate descent along two groups of variables: the coupling weights versus the project direction. We explain the rationale of the algorithm before presenting it formally.

We first address discrete distributions, followed by GMMs. Both cases involve transforming Fisher’s ratio into a Rayleigh-Ritz quotient. This conversion is simpler for discrete distributions but requires an approximation for GMMs. Although the former can be viewed algorithmically as a special case of the latter, conceptually they are distinct. Hence, we discuss the derivation of the Rayleigh-Ritz quotient in the two cases separately but, for conciseness, explain its maximization only in the context of GMMs.

2.2 Discrete distributions

Suppose the optimal couplings between \mathcal{Q}_k ’s, $\boldsymbol{\pi}^{(k_1, k_2)}$, $(k_1, k_2) \in \mathcal{I}_B \cup \mathcal{I}_W$, have been solved, that is, $\boldsymbol{\pi}^{(k_1, k_2)} \in \Pi_{k_1, k_2}$ is a byproduct of solving Eq. (1). Denote the collection of these couplings by $\Pi^* = \{\boldsymbol{\pi}^{(k_1, k_2)}, (k_1, k_2) \in \mathcal{I}_B \cup \mathcal{I}_W\}$. The between-class and within-class variations become

$$\bar{V}_B(A, \Pi^*) = \frac{1}{|\mathcal{I}_B|} \sum_{(k_1, k_2) \in \mathcal{I}_B} \sum_{i=1}^{m_{k_1}} \sum_{j=1}^{m_{k_2}} \pi_{i,j}^{(k_1, k_2)} \cdot \left\| A^t \cdot x_i^{(k_1)} - A^t \cdot x_j^{(k_2)} \right\|^2,$$

$$\bar{V}_W(A, \Pi^*) = \frac{1}{|\mathcal{I}_W|} \sum_{(k_1, k_2) \in \mathcal{I}_W} \sum_{i=1}^{m_{k_1}} \sum_{j=1}^{m_{k_2}} \pi_{i,j}^{(k_1, k_2)} \cdot \left\| A^t \cdot x_i^{(k_1)} - A^t \cdot x_j^{(k_2)} \right\|^2.$$

To stress the fact that the couplings in Π^* are assumed given, we use the notations $\bar{V}_B(A, \Pi^*)$ and $\bar{V}_W(A, \Pi^*)$. Let matrices C_B and C_W (of dimension $d \times d$) be

$$C_B = \frac{1}{|\mathcal{I}_B|} \sum_{(k_1, k_2) \in \mathcal{I}_B} \sum_{i=1}^{m_{k_1}} \sum_{j=1}^{m_{k_2}} \pi_{i,j}^{(k_1, k_2)} \cdot \left(x_i^{(k_1)} - x_j^{(k_2)} \right) \cdot \left(x_i^{(k_1)} - x_j^{(k_2)} \right)^t, \quad (6)$$

$$C_W = \frac{1}{|\mathcal{I}_W|} \sum_{(k_1, k_2) \in \mathcal{I}_W} \sum_{i=1}^{m_{k_1}} \sum_{j=1}^{m_{k_2}} \pi_{i,j}^{(k_1, k_2)} \cdot \left(x_i^{(k_1)} - x_j^{(k_2)} \right) \cdot \left(x_i^{(k_1)} - x_j^{(k_2)} \right)^t. \quad (7)$$

Lemma 1 *The between-class variation $\bar{V}_B(A, \Pi^*) = \text{tr}(A^t C_B A)$ and the within-class variation $\bar{V}_W(A, \Pi^*) = \text{tr}(A^t C_W A)$.*

The proof is in the Appendix A. In particular, if we optimize one projection direction a , $\text{tr}(a^t C_W a) = a^t C_W a$ and $\text{tr}(a^t C_B a) = a^t C_B a$. The Fisher’s ratio becomes

$$r(a, \Pi^*) = \frac{a^t C_B a}{a^t C_W a}. \quad (8)$$

2.3 Gaussian mixture models

In our discussion thus far, we have focused on discrete distributions. For continuous distributions, except for the Gaussian distribution, there is no closed form to compute the Wasserstein distance. The literature commonly addresses this challenge by approximating continuous distributions with empirical discrete distributions derived from samples. However, this approach is significantly limited by the curse of dimensionality, as discussed in several studies (Pele and Werman, 2009; Cuturi, 2013; Wang et al., 2023). Chen et al. (2019) introduced an innovative method: modeling a continuous distribution via a Gaussian Mixture Model (GMM) and defining the so-called *Minimized Aggregated Wasserstein* (MAW) distance. Under the MAW framework, a GMM is treated as a discrete distribution over Gaussian components, and the Wasserstein distance between these components is the counterpart of the Euclidean distance between support points in discrete distributions. The availability of a closed-form solution for the Wasserstein distance between Gaussian distributions has motivated the definition of MAW. Delon and Desolneux (2020) derived theoretical properties of MAW. In practice, this distance obviates the need for generating large samples from high-dimensional spaces. Lin et al. (2023) presents an application demonstrating this advantage. Furthermore, even in scenarios with high-dimensional data, the required number of components to accurately model data is often low, ensuring that the computation of MAW remains efficient.

Consider two Gaussian distributions ϕ_1 and ϕ_2 in \mathbb{R}^d , parameterized respectively by (μ_i, Σ_i) , $i = 1, 2$, where μ_i is the mean vector and Σ_i is the covariance matrix. The squared Wasserstein distance $W^2(\phi_1, \phi_2)$ is given by

$$W^2(\phi_1, \phi_2) = \|\mu_1 - \mu_2\|^2 + \text{tr} \left[\Sigma_1 + \Sigma_2 - 2 \left(\Sigma_1^{\frac{1}{2}} \Sigma_2 \Sigma_1^{\frac{1}{2}} \right)^{\frac{1}{2}} \right].$$

Suppose random vector $Z_1 \sim \phi_1$ and $Z_2 \sim \phi_2$. Let Π_{ϕ_1, ϕ_2} be the set of coupling distributions for Z_1 and Z_2 , that is, joint distributions on (Z_1, Z_2) with marginal distributions ϕ_1 and ϕ_2 . Then

$$W^2(\phi_1, \phi_2) = \min_{\pi \in \Pi_{\phi_1, \phi_2}} E_{\pi} \|Z_1 - Z_2\|^2.$$

An upperbound on $W^2(\phi_1, \phi_2)$ is obtained by setting π as $\hat{\pi}$ —the joint distribution of Z_1

and Z_2 under the independence assumption. Let

$$\widehat{W}^2(\phi_1, \phi_2) = E_{\hat{\pi}} \|Z_1 - Z_2\|^2.$$

Lemma 2 $\widehat{W}^2(\phi_1, \phi_2) = \|\mu_1 - \mu_2\|^2 + \text{tr}[\Sigma_1 + \Sigma_2] = \text{tr}[\Sigma_1 + \Sigma_2 + (\mu_1 - \mu_2) \cdot (\mu_1 - \mu_2)^t]$,
and $\widehat{W}^2(P(\phi_1, A), P(\phi_2, A)) = \text{tr}[A^t \cdot (\Sigma_1 + \Sigma_2 + (\mu_1 - \mu_2) \cdot (\mu_1 - \mu_2)^t) \cdot A]$.

The proof is in Appendix B. Now consider GMMs $\mathcal{G}_k = \{(p_i^{(k)}, \phi_i^{(k)}), i = 1, \dots, m_k\}$, $k = 1, \dots, n$, where $p_i^{(k)}$ is the prior probability on the i th component, and m_k is the number of components. As with the case of discrete distribution, let Π_{k_1, k_2} be the set of all couplings between the prior probabilities of \mathcal{G}_{k_1} and \mathcal{G}_{k_2} . Without loss of generality, the MAW distance between \mathcal{G}_{k_i} , $i = 1, 2$, is defined as follows:

$$\widetilde{W}^2(\mathcal{G}_{k_1}, \mathcal{G}_{k_2}) = \min_{\pi \in \Pi_{k_1, k_2}} \sum_{i=1}^{m_{k_1}} \sum_{j=1}^{m_{k_2}} \pi_{i,j} W^2(\phi_i^{(k_1)}, \phi_j^{(k_2)}).$$

For GMMs, we again define the Fisher's ratio using Eq. (4), but $\bar{V}_B(A)$ and $\bar{V}_W(A)$ are computed using the MAW distance (denoted by \widetilde{W}) instead of the Wasserstein distance (denoted by W). Under a given set of couplings between Gaussian components in different GMMs, denoted by Π^* , the between-class and within-class variations, i.e., $\bar{V}_B(A)$ and $\bar{V}_W(A)$, become, respectively,

$$\bar{V}_B(A, \Pi^*) = \frac{1}{|\mathcal{I}_B|} \sum_{(k_1, k_2) \in \mathcal{I}_B} \sum_{i=1}^{m_{k_1}} \sum_{j=1}^{m_{k_2}} \pi_{i,j}^{(k_1, k_2)} \cdot W^2(P(\phi_i^{(k_1)}, A), P(\phi_j^{(k_2)}, A)),$$

$$\bar{V}_W(A, \Pi^*) = \frac{1}{|\mathcal{I}_W|} \sum_{(k_1, k_2) \in \mathcal{I}_W} \sum_{i=1}^{m_{k_1}} \sum_{j=1}^{m_{k_2}} \pi_{i,j}^{(k_1, k_2)} \cdot W^2(P(\phi_i^{(k_1)}, A), P(\phi_j^{(k_2)}, A)).$$

For a Gaussian distribution $\phi \sim N(\mu, \Sigma)$, linear transform by matrix A yields a Gaussian distribution $P(\phi, A) \sim N(A^t \mu, A^t \Sigma A)$. Let $\tilde{\Sigma}_i^{(k)} = A^t \Sigma_i^{(k)} A$. Note that the squared Wasserstein distance between $P(\phi_i^{(k_1)}, A)$ and $P(\phi_j^{(k_2)}, A)$ is

$$W^2(P(\phi_i^{(k_1)}, A), P(\phi_j^{(k_2)}, A)) = \left\| A^t \cdot \mu_i^{(k_1)} - A^t \cdot \mu_j^{(k_2)} \right\|^2 + \text{tr} \left[\tilde{\Sigma}_i^{(k_1)} + \tilde{\Sigma}_j^{(k_2)} - 2 \left(\left(\tilde{\Sigma}_i^{(k_1)} \right)^{\frac{1}{2}} \tilde{\Sigma}_j^{(k_2)} \left(\tilde{\Sigma}_i^{(k_1)} \right)^{\frac{1}{2}} \right)^{\frac{1}{2}} \right]. \quad (9)$$

The calculation of $W^2(\phi_i, \phi_j)$ is more intensive than that of $\widehat{W}^2(\phi_i, \phi_j)$. However, this slight increase in computation is not the reason we approximate W^2 by \widehat{W}^2 . The second term in Eq. (9) for computing W^2 prevents us to convert Fisher's ratio $r(a) = \bar{V}_B(a, \Pi^*)/\bar{V}_W(a, \Pi^*)$ into a form of Rayleigh-Ritz quotient, as that in Eq. (8). It is thus difficult to maximize $r(a)$.

We propose to replace the true Wasserstein distance between Gaussian distributions by its upperbound \widehat{W} . Given the set of couplings Π^* , we approximate the Fisher's ratio $r(A, \Pi^*)$ by

$$\hat{r}(A, \Pi^*) = \frac{\widehat{V}_B(A, \Pi^*)}{\widehat{V}_W(A, \Pi^*)},$$

where

$$\begin{aligned}\widehat{V}_B(A, \Pi^*) &= \frac{1}{|\mathcal{I}_B|} \sum_{(k_1, k_2) \in \mathcal{I}_B} \sum_{i=1}^{m_{k_1}} \sum_{j=1}^{m_{k_2}} \pi_{i,j}^{(k_1, k_2)} \cdot \widehat{W}^2(P(\phi_i^{(k_1)}, A), P(\phi_j^{(k_2)}, A)), \\ \widehat{V}_W(A, \Pi^*) &= \frac{1}{|\mathcal{I}_W|} \sum_{(k_1, k_2) \in \mathcal{I}_W} \sum_{i=1}^{m_{k_1}} \sum_{j=1}^{m_{k_2}} \pi_{i,j}^{(k_1, k_2)} \cdot \widehat{W}^2(P(\phi_i^{(k_1)}, A), P(\phi_j^{(k_2)}, A)).\end{aligned}$$

Define

$$\begin{aligned}\hat{C}_B &= \frac{1}{|\mathcal{I}_B|} \sum_{(k_1, k_2) \in \mathcal{I}_B} \sum_{i=1}^{m_{k_1}} \sum_{j=1}^{m_{k_2}} \pi_{i,j}^{(k_1, k_2)} (\mu_i^{(k_1)} - \mu_j^{(k_2)}) \cdot (\mu_i^{(k_1)} - \mu_j^{(k_2)})^t \\ &\quad + \frac{1}{|\mathcal{I}_B|} \sum_{(k_1, k_2) \in \mathcal{I}_B} \left[\sum_{i=1}^{m_{k_1}} p_i^{(k_1)} \Sigma_i^{(k_1)} + \sum_{j=1}^{m_{k_2}} p_j^{(k_2)} \Sigma_j^{(k_2)} \right],\end{aligned}\tag{10}$$

$$\begin{aligned}\hat{C}_W &= \frac{1}{|\mathcal{I}_W|} \sum_{(k_1, k_2) \in \mathcal{I}_W} \sum_{i=1}^{m_{k_1}} \sum_{j=1}^{m_{k_2}} \pi_{i,j}^{(k_1, k_2)} (\mu_i^{(k_1)} - \mu_j^{(k_2)}) \cdot (\mu_i^{(k_1)} - \mu_j^{(k_2)})^t \\ &\quad + \frac{1}{|\mathcal{I}_B|} \sum_{(k_1, k_2) \in \mathcal{I}_W} \left[\sum_{i=1}^{m_{k_1}} p_i^{(k_1)} \Sigma_i^{(k_1)} + \sum_{j=1}^{m_{k_2}} p_j^{(k_2)} \Sigma_j^{(k_2)} \right].\end{aligned}\tag{11}$$

Lemma 3 *The between-class variation $\widehat{V}_B(A, \Pi^*) = \text{tr}(A^t \hat{C}_B A)$ and the within-class variation $\widehat{V}_W(A, \Pi^*) = \text{tr}(A^t \hat{C}_W A)$.*

The proof is in Appendix C. Based on Lemma 3,

$$\hat{r}(a, \Pi^*) = \frac{a^t \hat{C}_B a}{a^t \hat{C}_W a},\tag{12}$$

which is the Rayleigh-Ritz quotient. We note that although \widehat{W} is used to replace the Wasserstein distance to maximize $\hat{r}(a, \Pi^*)$, the set of couplings Π^* in each iteration is obtained from the calculation of the MAW distance between two GMMs.

The ratio in Eq. (8) or Eq. (12) is essentially the Rayleigh-Ritz quotient with matrices C_B (or \hat{C}_B) and C_W (or \hat{C}_W). Without loss of generality, we discuss in terms of \hat{C}_B and \hat{C}_W . Note that both matrices are semi-positive definite, and in practice, usually positive definite. Here, \hat{C}_B and \hat{C}_W play a similar role as the between-class covariance and within-class covariance matrix in LDA. The solution to Fisher's optimization applies likewise. Specifically, let $\hat{C}_W = \left(\hat{C}_W^{\frac{1}{2}}\right)^t \cdot \hat{C}_W^{\frac{1}{2}}$ and $\hat{C}_B^* = \left(\hat{C}_W^{-\frac{1}{2}}\right)^t \hat{C}_B \hat{C}_W^{-\frac{1}{2}}$. Use change of variables and define $b = \hat{C}_W^{\frac{1}{2}} \cdot a$. Then Fisher's ratio becomes

$$r(b, \Pi^*) = \frac{b^t \hat{C}_B^* b}{b^t b},$$

which is maximized using eigen-decomposition of \hat{C}_B^* . Assume that the eigenvalues are in descending order and the corresponding eigenvectors are $(v_1^*, v_2^*, \dots, v_d^*)$. Then $b = v_1^*$ maximizes $r(b, \Pi^*)$. Consequently, $a = \hat{C}_W^{-\frac{1}{2}} \cdot v_1^*$ maximizes $r(a, \Pi^*)$.

In light of the above discussion, we iterate between computing couplings $\boldsymbol{\pi}^{(k_1, k_2)}$, $(k_1, k_2) \in \mathcal{I}_B \cup \mathcal{I}_W$ given a and optimizing a under the given couplings. The solution of squared MAW distances $\widehat{W}^2(P(\mathcal{G}_{k_1}, a), P(\mathcal{G}_{k_2}, a))$ includes $\boldsymbol{\pi}^{(k_1, k_2)}$'s. For discrete distributions, the squared Wasserstein distances $W^2(P(\mathcal{Q}_{k_1}, a), P(\mathcal{Q}_{k_2}, a))$ are computed instead.

To start the iteration, we initialize $\boldsymbol{\pi}^{(k_1, k_2)}$'s based on the original data (no dimension reduction). The two index sets \mathcal{I}_B and \mathcal{I}_W are pre-selected. We will provide a brief explanation of the method used to determine \mathcal{I}_B and \mathcal{I}_W shortly.

Similarly as with the conventional Fisher's optimization, if the reduced dimension is more than one, we let $b_i = v_i^*$, $i = 1, \dots, d'$, where $d' < d$ is the desired dimension. The b_i 's are orthonormal. Following the terminology in LDA, we define

$$a_i = C_W^{-\frac{1}{2}} \cdot b_i. \quad (13)$$

as the *discriminant coordinates* or *canonical variates* axes.

In contrast to Fisher's classical solution for LDA, the discriminant coordinates a_i in our approach are not computed by a closed form but are instead updated iteratively in

tandem with the coupling weights. Consider the scenario where $d' > 1$. In this case, we define the matrix A as $A = (a_1, \dots, a_{d'})$. Next, we compute the projection $P(\mathcal{Q}_k, A)$ for each $k = 1, \dots, n$. These projections are then used to calculate pairwise Wasserstein distances and to update the couplings in Π^* , based on which A will be updated again. When an orthonormal projection is required, the OTAF method is adjusted accordingly. Specifically, after determining $a_i, i = 1, \dots, d'$, an orthonormal span for the subspace spanned by a_i 's is identified and the orthonormal basis are taken as a_i 's instead.

We now describe the method for determining the index sets \mathcal{I}_B and \mathcal{I}_W , which correspond to between-class and within-class pairs, respectively. For each instance $\mathcal{G}_k, k = 1, \dots, n$, we calculate its average squared MAW distance (in the original dimension) to every other instance within the same class, denoted as δ_k . Additionally, we compute its average squared MAW distance to instances from different classes, denoted as δ'_k . Define *discriminant distance ratio* $\gamma_k = \delta'_k / \delta_k$. A higher γ_k value indicates that \mathcal{G}_k is, on average, more distant from instances in different classes compared to those in the same class, suggesting that \mathcal{G}_k is easier to classify. Rather than considering all pairs $(\mathcal{G}_{k_1}, \mathcal{G}_{k_2})$, we focus on the more challenging cases as indicated by γ_k . We rank γ_k 's and select a specific proportion—say, α percent—of the values with the smallest γ_k . In our experiment, we set α to 1/3. We denote the set of selected k values as \mathcal{K}_α . For simplicity, define $\mathcal{K} = \{1, \dots, n\}$. Then $\mathcal{I}_B = \{(k_1, k_2) : k_1 \in \mathcal{K}_\alpha, k_2 \in \mathcal{K}, Y_{k_1} \neq Y_{k_2}\}$, and $\mathcal{I}_W = \{(k_1, k_2) : k_1 \in \mathcal{K}_\alpha, k_2 \in \mathcal{K}, Y_{k_1} = Y_{k_2}\}$.

2.4 A unified algorithm

Next, we articulate the OTAF algorithm in a manner applicable to both discrete distributions, as per the Wasserstein distance, and GMMs, as per the MAW distance. To streamline the discussion, we equate a discrete distribution $\{(p_i, x_i), i = 1, \dots, m\}$ to a GMM with m components, $\{(p_i, \phi_i), i = 1, \dots, m\}$, where p_i represents the prior probability of the i -th component, and ϕ_i is a Gaussian distribution with mean $\mu_i = x_i$ and a zero covariance matrix $\Sigma_i = \mathbf{0}$. In this representation, the MAW distance between GMMs aligns with the Wasserstein distance between discrete distributions. Importantly, when the covariance ma-

trices are entirely degenerated, we have $W^2(\phi_i, \phi_j) = \widehat{W}^2(\phi_i, \phi_j) = \|\mu_i - \mu_j\|^2$, that is, the Wasserstein distance $W(\phi_i, \phi_j)$ and the upperbound distance $\widehat{W}(\phi_i, \phi_j)$ for the Gaussian distributions are identical to the Euclidean distance between the mean vectors $\|\mu_i - \mu_j\|$. Moreover, with $\Sigma_i = \mathbf{0}$, \hat{C}_B and \hat{C}_W in Eqs. (10) and (11) simplify to C_B and C_W in Eqs. (6) and (7), respectively, since the second terms in Eqs. (10) and (11) vanish. In summary, treating the support points of a discrete distribution as degenerated Gaussian components does not alter the algorithm. We thus describe the OTAF algorithm, presented in Algorithm 1, for GMMs.

Algorithm 1: OTAF

Input: A collection of GMMs $\mathcal{G}_k = \{(p_i^{(k)}, \phi_i^{(k)}), i = 1, \dots, m_k\}$, $k = 1, \dots, n$, where $\phi_i^{(k)} \sim N(\mu_i^{(k)}, \Sigma_i^{(k)})$, and their class labels Y_k , $k = 1, \dots, n$; Hyperparameters: d' (the reduced dimension), κ (the minimum number of iterations), $\bar{\kappa}$ (the maximum number of iterations), ϵ (threshold for termination, e.g., $1.0e - 4$).

- 1: Determine \mathcal{I}_B and \mathcal{I}_W based on the discriminant distance ratios (Section 2.2).
- 2: $\mathbf{I}_{d \times d} \rightarrow A$, where $\mathbf{I}_{d \times d} \in \mathbb{R}^{d \times d}$ is the identity matrix.
- 3: $1 \rightarrow \tau$, $\infty \rightarrow \eta$, compute the Fisher's ratio $r(A)$, $r(A) \rightarrow \rho^\tau$.
- 4: **while** $\tau < \kappa$ or $(\eta > \epsilon$ and $\tau < \bar{\kappa})$ **do**
- 5: Compute the projected GMMs: $P(\mathcal{G}_k, A)$, $k = 1, \dots, n$. Solve the OT couplings $\pi^{(k_1, k_2)}$ for $P(\mathcal{G}_{k_1}, A)$ and $P(\mathcal{G}_{k_2}, A)$, $(k_1, k_2) \in \mathcal{I}_B \cup \mathcal{I}_W$.
- 6: Compute \hat{C}_B by Eq. (10) and \hat{C}_W by Eq. (11). Let $(\hat{C}_W^{-\frac{1}{2}})^t \hat{C}_B \hat{C}_W^{-\frac{1}{2}} \rightarrow C_B^*$.
- 7: Solve the eigenvectors $(v_1^*, v_2^*, \dots, v_d^*)$ of C_B^* (eigenvalues in descending order). Let $\hat{C}_W^{-\frac{1}{2}} \cdot v_i^* \rightarrow a_i$, $i = 1, \dots, d'$.
- 8: If orthonormal basis is required, set A to be the orthonormal basis for the span of $(a_1, \dots, a_{d'})$, otherwise $(a_1, \dots, a_{d'}) \rightarrow A$.
- 9: $\tau + 1 \rightarrow \tau$
- 10: Compute $r(A)$, $r(A) \rightarrow \rho^\tau$, and $(\rho^\tau - \rho^{\tau-1})/\rho^{\tau-1} \rightarrow \eta$.
- 11: **end while**

return Projection matrix A , $A \in \mathbb{R}^{d \times d'}$.

To establish a criterion for terminating the iterative process, we evaluate Fisher's ratio

$r(A)$ in each round and compare the previous A with the current updated one. The iteration is stopped when the relative increase in this ratio falls below a predetermined threshold, for instance, 10^{-4} . Empirical evidence from our experiments indicates that convergence under this criterion typically occurs at a rapid pace.

To better understand the theoretical underpinnings of the OTAF algorithm, we focus on the simpler scenario of discrete distributions and the optimization process for a single direction $a \in \mathbb{R}^d$. By its definition, $r(a) = r(a, \Pi^*)$, where Π^* is the set of optimal couplings under the projection a . A theoretical challenge comes from the fact we cannot definitively assert that Π^* is the maximizer of $r(a, \Pi)$ for all feasible coupling sets Π . It is evident that $\bar{V}_B(a) = \bar{V}_B(a, \Pi^*) \leq \bar{V}_B(a, \Pi)$, and similarly, $\bar{V}_W(a) = \bar{V}_W(a, \Pi^*) \leq \bar{V}_W(a, \Pi)$. Yet, the inequality $r(a, \Pi^*) \geq r(a, \Pi)$, where $r(a, \Pi) = \bar{V}_B(a, \Pi)/\bar{V}_W(a, \Pi)$, may not hold.

In the Appendix D, we establish a relatively modest result pertaining to this issue, which is stated in Theorem 1. In practical applications, especially when the reduced dimension $d' > 1$, we typically observe that the algorithm converges swiftly after a few iterations, followed by minor oscillations over an extended period. In contrast, for $d' = 1$, the algorithm shows a consistent ascending trend and reaches convergence rapidly. This phenomenon and its implications are thoroughly examined in Section 3.5.

Theorem 1 *For discrete distributions, if we assume $r(a) \geq r(a, \Pi)$, where Π contains valid couplings, the OTAF algorithm for maximizing $r(a) = \frac{\bar{V}_B(a)}{\bar{V}_W(a)}$, $a \in \mathbb{R}^d$, is ascending after every round of updating the couplings and direction a .*

In the case of GMMs, as the Wasserstein distance between Gaussian components is replaced by its upper bound, it is even harder to provide a theoretical guarantee for the algorithm. We will again investigate the convergence characteristic of the algorithm in this scenario via experiments.

3 Experiments

To perform classification based on pairwise distances alone, we employ the kernel version of the pseudo-mixture model developed by Qiao and Li (2016). For each class l , $l = 1, \dots, M$, a

pseudo-density denoted by \mathcal{M}_l is formed based on distances. Essentially, a pseudo-density is a conceptually formulated density function on a metric space, on the notion of distance-preserving mapping from a metric space to a Euclidean space, as detailed in the work of (Qiao and Li, 2016). Suppose the GMMs in a class are \mathcal{G}_j , $j \in \mathcal{I}_l$, where \mathcal{I}_l is a set of indices containing the instances that belong to class l . The pseudo-density computed at a GMM \mathcal{G} is

$$\psi(\mathcal{G} | \mathcal{M}_l) = \sum_{j \in \mathcal{I}_l} \frac{1}{|\mathcal{I}_l|} \left(\frac{1}{\sqrt{\pi b}} \right)^{2s} e^{-\frac{\tilde{w}^2(\mathcal{G}, \mathcal{G}_j)}{b}}, \quad (14)$$

where s is a shape parameter and b is a scale parameter, both are shared across the classes. Details on the estimation of s and b are referred to (Qiao and Li, 2016). Suppose the prior probabilities of class l is α_l , $\sum_{l=1}^M \alpha_l = 1$. Then the posterior probability for class l is $P(Y = l | \mathcal{G}) \propto \alpha_l \psi(\mathcal{G} | \mathcal{M}_l)$. If dimension reduction is applied, we need to replace \mathcal{G} and \mathcal{G}_j 's by the marginal distributions in the reduced dimensions.

3.1 Data Preparation

Our experiments involve three datasets, each comprising instances that contain a set of data points. For example, an instance can be a patient characterized by a set of feature vectors, each containing measurements of individual cells in the patient's tissue sample. Typically, a tissue sample from one patient contains numerous cells. In conventional machine learning studies, an instance is represented by a single feature vector. To clarify this distinction, we describe each instance as a "data cloud." In the discussion below, the terms "data cloud" and "subject" are both used; the former emphasizes the data format, while the latter is more commonly used in a biomedical context.

Each data cloud is processed and effectively characterized using a GMM. The GMM representation for a data cloud varies depending on the method used to generate the mixture model and the number of components assumed. We investigate multiple schemes and different numbers of components. Consequently, for each original dataset, several collections of GMMs are created, each serving as a dataset in our experiments. Specifically, we begin with three original datasets, each of which generates eight collections of GMMs. Therefore, our method is tested on a total of 24 datasets containing GMMs as instances.

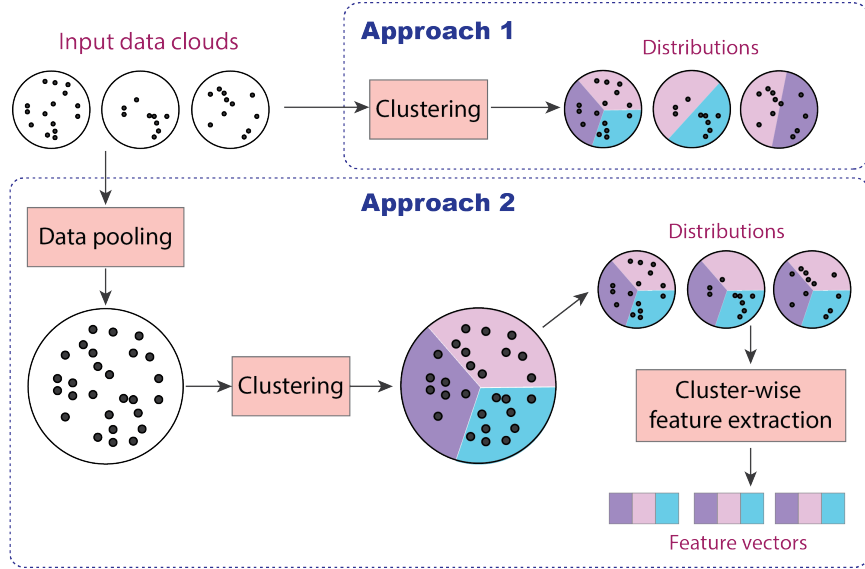


Figure 1: Two approaches for representing data clouds. Approach 1: data points in each instance (a data cloud) are clustered separately. Approach 2: data points in all instances are pooled and clustered together with coherent cluster labels assigned. Cluster-wise feature extraction can be performed to create vector representations.

For every subject in the study, we generated eight different GMMs using two primary clustering approaches: the “separate” method and the “combined” method. These two approaches, the former being “Approach 1” and the latter “Approach 2”, are illustrated in Figure 1. In the combined approach, cells from all subjects are pooled into a single dataset, which is then subjected to clustering. This results in consistent cluster labels across all subjects. For each subject, we estimate the Gaussian mean and covariance for each cluster based on the assigned cluster labels to their data points, subsequently forming the GMM. The proportion of points in a cluster is taken as the prior probability of the corresponding Gaussian component. It is important to note that some subjects might not have data points in certain clusters; these clusters only contain points from other subjects. Consequently, the number of Gaussian components for such a subject will be fewer than the total number of clusters identified in the combined dataset. On the other hand, in the separate method, we perform clustering on the points within each subject individually. After clustering, the GMM is formed likewise.

In both the combined and separate clustering schemes, we set the number of components in the GMMs as 3, 5, 7, and 10. For the brevity of discussion, denote the number of components in a GMM by ζ . We also adopt the following naming convention. Take GMM-C-3 as an example. It refers to a GMM with $\zeta = 3$ which is obtained by the combined clustering scheme. In contrast, GMM-S-3 indicates that the separate clustering scheme is used. If a subject’s point count is relatively low, we adjust the number of components to a smaller value than the initially set number. While our method is also applicable to discrete distributions (considered as a special case of GMMs in our algorithm description), directly working with the entire data cloud of each subject is often impractical due to the vast number of points in each cloud. Clustering serves not only to reduce computational demands in subsequent processes but also to enhance the robustness of the analysis against noise in the data. The clusters thus formed can often provide a more effective representation of the original data cloud. However, the application of clustering brings its own set of challenges. A common difficulty lies in determining the optimal number of components for a GMM. Therefore, it is beneficial to have methodologies that remain robust despite variations in the GMM representation. To address this, we generated GMMs with varying numbers of components and evaluated the prediction accuracy of each model across different algorithms in our experiments.

By using both combined and separate clustering schemes in our study, we can compare our method with traditional vector-based approaches. In conventional machine learning applications for vector data, a frequent strategy for handling data clouds involves transforming them into vectors. This is typically done by clustering and ensuring consistent cluster labels across different subjects, as demonstrated in Figure 1. Features such as the proportion of each cluster and the mean measurements of points within a cluster are compiled into a single feature vector. To maintain coherence of cluster labels across different subjects, it is essential that the clusters be either algorithmically aligned or inherently aligned. However, algorithms used for cluster alignment can introduce errors. To circumvent this potential issue, we employed clustering on the combined data from all subjects, thereby inherently aligning the clusters without the need for an additional alignment algo-

rithm. This approach ensures uniform cluster labels across different subjects, facilitating a more accurate comparison with conventional vector-based methods.

In practical scenarios, factors such as privacy concerns may render the pooling of data for clustering infeasible. Additionally, there are inherent limitations to data pooling. For instance, when applying a learned prediction function to a new test subject, the data points of this subject must be clustered according to the same partitioning rules derived from the training data. This necessitates storing the partitioning rules as part of the learned model, which can be cumbersome. Moreover, from a learning perspective, clustering each subject’s data separately is often more effective in capturing distributions that are specifically tailored to each individual subject. For example, if a patient has a unique, small subset of cells, separate clustering is more likely to identify and characterize this distinct group. In contrast, when cells from all patients are clustered together, such a small group may be overshadowed or its members might be misclassified as outliers in other larger clusters. This highlights the importance of considering individual patient variability in the clustering process to ensure that unique characteristics are not overlooked. As will be discussed below, these aforementioned limitations of data pooling and aligned clustering have been reflected by experimental results.

3.2 Evaluation Method

In our study, given the limited number of subjects across all datasets, we evaluated performance using leave-one-out classification accuracy and Area Under Curve (AUC), both in the range of $[0, 1]$ with a higher value indicating better performance. We compared these results with several established classification algorithms: Support Vector Machine (SVM), Random Forest (RF), and Logistic Regression (LR). Our proposed method is referred to as *Canonical Variates in Wasserstein space* (CVW), with two variants: CVW-C, applying CVW to Gaussian Mixture Models (GMMs) created using the combined clustering approach, and CVW-S, employing CVW with GMMs derived from the separate clustering scheme. The CVW method first apply the OTAF algorithm to reduce the dimension to a specified value. Then we form the pseudo-mixture model in Eq. (14) based on the Wasser-

stein distance between GMMs in the dimension reduced space. For one dataset, we also evaluated performance of the pseudo-mixture model in the original space. We refer to this method simply as *Pseudo-Mixture Model* (PMM).

Based on clustering applied to the combined data, for each subject, we constructed feature vectors by concatenating the proportion of each cluster and the average values of variables over points within the cluster. In the case when a subject has a missing cluster, we set the corresponding proportion to zero and the cluster mean to the mean over the entire data. We also explored using only cluster proportions or only cluster means as features. The performance based on different types of feature vectors varies depending on the dataset, so we will report the best results from these three types. Specific dataset results and their detailed analysis will be presented later. For the SVM, RF, and LR algorithms, we experimented with various hyperparameters and will report only the highest-performing configurations for each algorithm. This approach allows for a fair and effective comparison of our CVW method against these widely-used classification techniques.

3.3 Pulmonary fibrosis data analysis

We experiment with a single-nucleus sequencing data of (Habermann et al., 2020) related to pulmonary fibrosis (PF). This dataset comprises 20 cases and 10 controls. A recent publication has highlighted that the majority of significant signals are observed in epithelial cell types, specifically SCG3A2+, AT2, Basal, MUC5B+, and AT1 Zhang and Guo (2022). In our analysis, we focus on SCG3A2+ cell types. We downloaded the data from https://github.com/mqzhanglab/BSDE_pipeline/tree/main/data. The number of SCG3A2+ cells per individual subject ranges from 1 to 663. Since the number of cells is relatively small, we select the top 30 highly variable genes for our analysis. If the number of cells per sample is below 10, we model the cells by a single 30-dimensional Gaussian distribution, so the sample mean and covariance of the cells are the estimates of the Gaussian mean and covariance matrix. For the case where there is only one cell in the sample, we use that cell as the estimate of the Gaussian mean, and estimate the covariance by the sample covariance matrix of ten perturbed sample points generated by adding to that point Gaussian noise

(zero mean and standard deviation 0.1), similarly as the practice in Lin et al. (2023). Otherwise, we construct a GMM for the sample based on k-means clustering, as explained in the previous subsection.

In Figure 2(a), we compare the performance in terms of classification accuracy and AUC achieved by CVW and PMM across different numbers of Gaussian components and the two schemes of clustering (CVW-C versus CVW-S). For PMM, performance based on GMM-S’s (separate clustering) is better than that from GMM-C’s (combined clustering). This observation may be attributed to better fitting of GMM by separate clustering. When dimension reduction is applied, however, the difference in AUC or accuracy becomes negligible. We also note that for both PMM and CVW, the performance is stable across different number of components in the GMM. In addition, dimension reduction to a single dimension yields consistently better results than classification in the original dimension. The improvement is remarkable in terms of accuracy. By AUC, the improvement from dimension reduction is most noticeable for GMMs formed based on combined clustering.

In Figure 2(b), we compare CVW-S and CVW-C with LR, RF, and SVM. Note that the GMMs used by LR, RF, and SVM are of the GMM-C type, the same as those used by CVW-C. We found that for LR, RF, and SVM, using both the proportions and the means yield on average the best performance. Hence we only report results in this case. For SVM, linear kernel is the best among RBF and polynomial at degree 3. For LR, we use elastic net to estimate the logistic model. In terms of AUC, SVM performs clearly worse than the other three approaches, and it is most sensitive to the number of components in GMMs. In terms of accuracy, LR performs the worst. In terms of AUC, LR, CVW-S, and CVW-C achieve similar results. As shown in the legends on the right hand side of the plots, when averaged over $\zeta \in \{3, 5, 7, 10\}$, CVW-S achieves the highest AUC. In terms of average accuracy, CVW-S and CVW-C reach the same level, and are considerably better than that by SVM (the second best). As shown by the standard deviation of the AUC or accuracy in the parenthesis, all the algorithms perform stably when ζ changes.

To further study the sensitivity of CVW to the number of components in GMM, we conduct the following study where the GMMs of training and test subjects have different

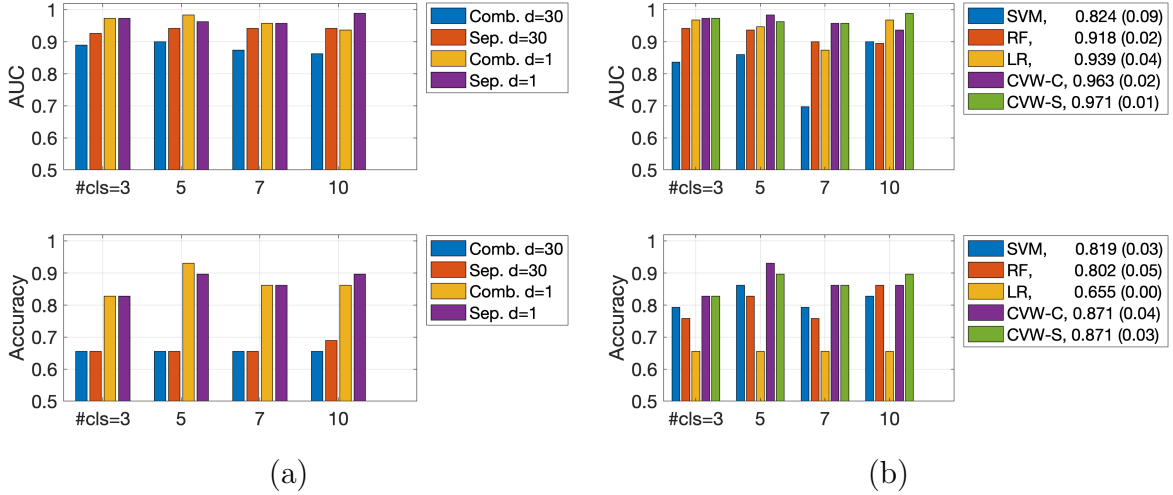


Figure 2: Performance comparison based on AUC and classification accuracy. (a) Results obtained from GMMs generated by the combined clustering and separate clustering schemes. The number of components in GMMs varies over $\{3, 5, 7, 10\}$. The original dimension is 30. With dimension reduction, one canonical variate is used. (b) Results obtained by vector-based algorithms SVM, RF, and LR are compared with CVW-C and CVW-S. In the legends on the right hand side of the plot, the average performance over the four different numbers of components is shown for each algorithm, and the value inside the parenthesis is the standard deviation.

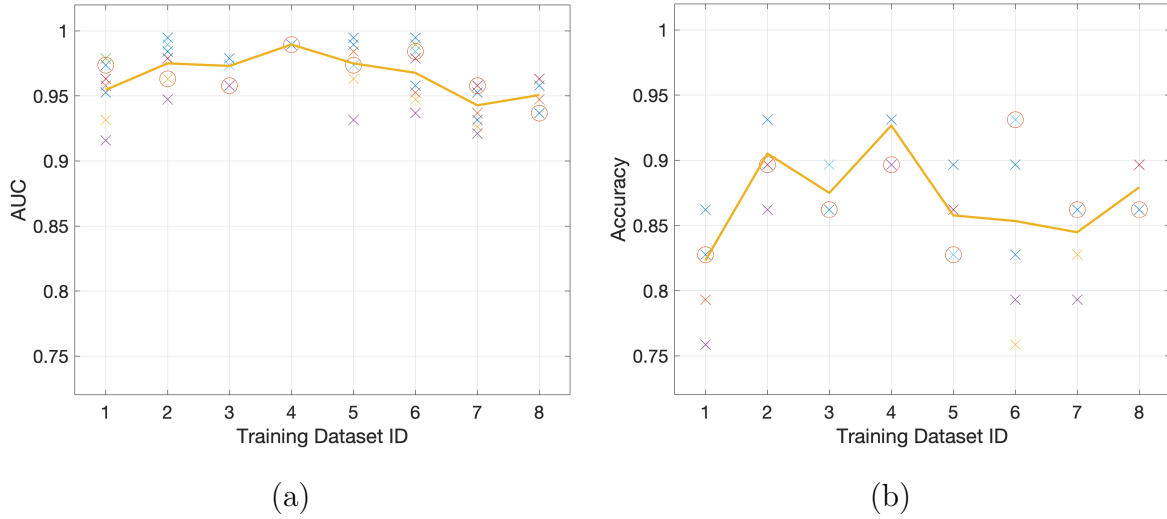


Figure 3: Examine the robustness of CVW when GMM representations of training and test data are generated under different setups. (a) AUC; (b) Classification accuracy. There are 8 datasets each contain GMMs created under a specific setup. Each dataset is used once for training, and for any given training dataset, the test data are taken from the 8 datasets respectively. The horizontal axis shows the training dataset ID, while at each training data set, AUCs or accuracy levels based on the 8 different test datasets are shown. When training and test samples are from the same dataset, the result is shown by a circled cross.

numbers of components and are generated by different clustering schemes. Denote the collections of GMM-S- ζ 's, $\zeta = 3, 5, 7, 10$, respectively by \mathbb{D}_i , $i = 1, \dots, 4$ and the collections of GMM-C- ζ 's, $\zeta = 3, 5, 7, 10$ by \mathbb{D}_i , $i = 5, \dots, 8$. Take \mathbb{D}_1 as an example. In leave-one-out evaluation, we trained our model using GMMs in \mathbb{D}_1 , leaving out one patient. We then applied this model to the left-out patient represented by a GMM from each \mathbb{D}_i , $i = 1, \dots, 8$. So for any given \mathbb{D}_i , we obtained 8 evaluation results, each corresponding to which \mathbb{D}_j the test data come from. The results are shown in Figure 3 (left plot for AUC and right plot for accuracy). For each training data \mathbb{D}_i , we also computed the average performance over all test data \mathbb{D}_j 's (the solid lines in the plots). In addition, when the training \mathbb{D}_i and test \mathbb{D}_j match, that is, $i = j$, we indicate the performance by a circle in the plots. As shown in the figure, the mismatch between the training \mathbb{D}_i and testing \mathbb{D}_j does not cause much difference in performance, especially viewed from an average sense. Sometimes, the mismatched test data even yield slightly better results than the matched test data.

Results summarized in Figure 3 further demonstrate that CVW is robust even when the number of components in GMM differs between training and test sets. Importantly, they also indicate a remarkable advantage of CVW over vector-based classification methods. In order to apply vector-based classification algorithms, the patients in both training and test sets must have the same number of clusters which are also aligned. In contrast, CVW can be applied as long as the patients are represented by GMMs. This flexibility allows us to cluster training and test data independently without restriction on the number of components. As shown by Figure 3, when the setups for creating the GMMs differ between training and test subjects, the influence on classification performance is marginal.

3.4 Breast cancer and uveal melanoma data analysis

In this section, we present our analyses of two additional datasets. We first downloaded single-cell data from a total of 26 breast cancer patients, with 16 of them diagnosed as either ER+ (luminal) or HER2+ and the remaining 10 diagnosed as TNBC (triple negative breast cancer) (Wu et al., 2021). Refer to this dataset at BC. In our analysis, TNBC is taken as class 1 and the other two types are class 0. Wu et al. (2021) investigated the cel-

lular heterogeneity of scRNA-seq data obtained from pre-treatment tumors of 26 patients. Their analysis unveiled significant heterogeneity in epithelial, immune, and mesenchymal phenotypes within each tumor. At least nine major cell types were identified, falling into 49 distinct cell subsets at high resolution. In our analysis, we aim to explore whether these diverse cell types can contribute to predicting cancer types in patients.

The second dataset is from the study of uveal melanoma (UM), a highly metastatic cancer largely unresponsive to treatment, including checkpoint immunotherapy. UMs can be further classified into two classes using a widely adopted 15-gene expression profile (GEP) test. Class 1 UMs are associated with a low metastatic risk, while class 2 UMs carry a high risk of metastasis. A recent paper has performed a single-cell analysis of UMs and identified potential discriminative features among tumor cells between class 1 and 2 UMs (Durante et al., 2020). We downloaded the scRNA-seq of tumor cells from 11 tumor samples, 3 in class 1 and the remaining in class 2. Similarly, in this paper, we would like to study whether the scRNA-seq data can contribute to predicting UM classes. For both datasets, we select the top 100 highly variable genes and derive the GMM for each patient following a similar approach as in the previous example.

We show the performance on BC data in Figure 4(a), (b). The left panel shows AUC and classification accuracy obtained with a varying number of canonical variates, using GMM-S-7's. The plot shows that the best AUC and accuracy are achieved in the range from 38 to 42, and in terms of both measures, CVW significantly outperforms PMM without dimension reduction. In the right panel, we compare results obtained from SVM, RF, LR, CVW-C, and CVW-S. For the first three vector-based methods, we use per-cluster proportions and mean vectors as features. Results are shown for GMMs with $\zeta = 3, 5, 7,$ and 10. The number of canonical variates is set to 40. In the legend on the right hand side, the average AUCs or accuracy levels across ζ for each algorithm are listed with the standard deviation in parenthesis. On average, CVW-C and CVW-S perform similarly with the former slightly better in AUC and the latter slightly better in accuracy; and they both outperform the other algorithms. By AUC, SVM performs similarly as CVW, but the standard deviation shows that SVM's results vary more dramatically when ζ changes.

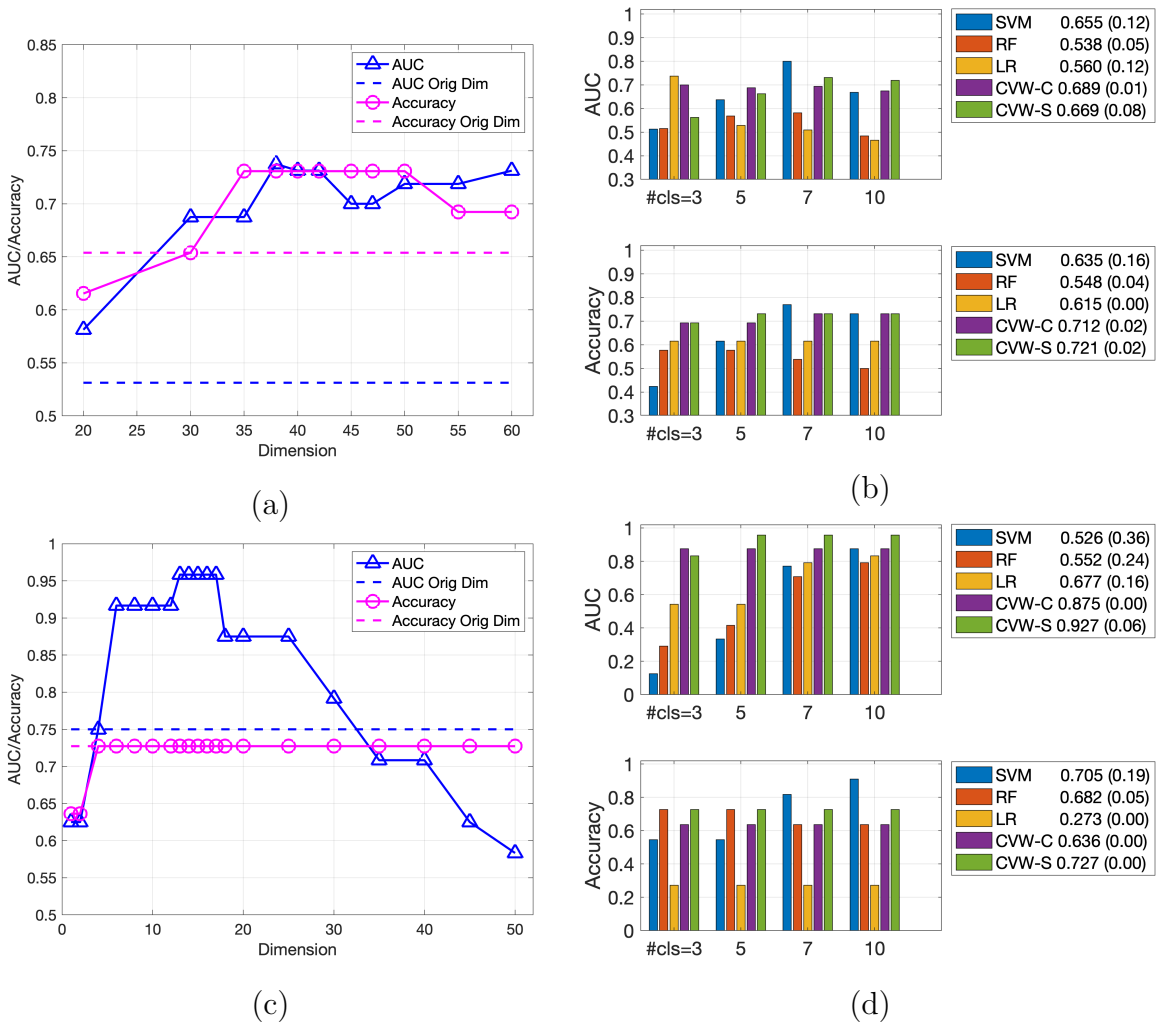


Figure 4: Classification performance on breast cancer (BC) and un_melanoma (UM) data. Top row: BC. Bottom row: UM. (a) and (c): Results across different numbers of canonical variates for GMM-S with $\zeta = 7$; (b) and (d): Compare SVM, RF, LR, CVW-C, and CVW-S over $\zeta \in \{3, 5, 7, 10\}$. In the legends on the right hand side, average AUCs and accuracy levels across ζ 's with standard deviation is listed.

Similarly we show the performance on UM data in Figure 4(c) and (d). The plot on the left is based on GMMs with $\zeta = 7$ obtained by the separate clustering scheme. It shows that when the number of canonical variates is in the range of 13 to 17, AUC is the best, while the accuracy stays at the same level all across. We compare CVW-S and CVW-C with SVM, RF, and LR in the plot on the right. For CVW-S, we use 13 canonical variates, while for CVW-C, one canonical variate is used. For RF and LR, the feature vectors contain per-cluster proportions and mean vectors. For SVM, the feature vectors contain only per-cluster proportions because this choice yields much better results. Based on the average performance shown in the legends on the right hand side, CVW-S outperforms all other algorithms by both AUC and accuracy. In addition, the standard deviation is small across different values of ζ . In contrast, SVM shows much high standard deviation in terms of AUC and accuracy.

3.5 Study of descending and convergence properties

To study the convergence behavior of the OTAF algorithm, we monitored Fisher’s ratio across iterations and calculated the Grassmann distance between the subspaces identified in consecutive iterations (specifically, comparing iteration τ with iteration $\tau - 1$ starting from $t = 2$). We refer to (Ye and Lim, 2016) for the definition of Grassmann distance. For each dataset, we conducted experiments using GMM-S- ζ , $\zeta = 3, 5, 7, 10$. The results for each ζ value are represented as individual curves in the plots of Figure 5. The plots in Figure 5(a), (b), (c) correspond to orthonormal projections, while those in Figure 5(d), (e), (f) correspond to non-orthonormal projections. For the IP dataset, where dimensionality is reduced to one, there is no distinction between orthonormal and non-orthonormal projections. Therefore, for non-orthonormal projections, we present results only for the BC and UM datasets. In the case of the UM dataset, we offer findings for two different numbers of canonical variates.

Several observations are noted from our study. Regarding Fisher’s ratio, we observe rapid convergence; typically, the ratio stabilizes after just a few iterations. However, an increase in d tends to introduce a minor degree of oscillation. The Grassmann distance

suggests that the identified subspace undergoes slight variations. Except for the PF data (reduced to $d = 1$), the Grassmann distance does not converge to zero, indicating continual changes in the subspace structure, possibly oscillation between spaces. When comparing orthonormal with non-orthonormal projections, the latter exhibits a somewhat lower level of oscillation, yet the Grassmann distance remains above zero. Interestingly, we found that orthonormal projections generally yield better classification results.

Given that the objective of identifying canonical variates is to enhance classification rather than serving as the final goal, we investigated how the oscillations depicted in Figure 5 impact classification performance. Focusing on the BC and UM datasets, we analyzed how AUC achieved by the canonical variates varies with the number of iterations. The results, corresponding to the GMM-S- ζ , $\zeta = 3, 5, 7, 10$ are provided in Figure 6. Our observations indicate that the AUC often attains a near-optimal value within just two or three iterations. Beyond this point, while the performance for the BC dataset shows some fluctuation with additional iterations, it generally remains stable for the UM dataset. This suggests that while the number of iterations can influence classification performance, particularly in the case of the BC data, the effect is relatively modest.

4 Conclusions and Discussions

In this paper, we have adapted the principle of Fisher’s ratio to the context of the Wasserstein metric space and formulated the problem of finding canonical variates. We introduce a new algorithm designed to optimize Fisher’s ratio and validate its efficacy using three real-world datasets. Our method uses pairwise distances between instances, a technique that, while offering significant benefits, is computationally intensive due to the necessity of calculating pairwise Wasserstein distances. However, it is worth noting that this process is embarrassingly parallelizable. Importantly, by utilizing pairwise distances, we can easily adjust which instances to consider, thereby focusing on those that are more difficult to classify—a strategy valuable for improving classification performance.

To further reduce the computational load, we can explore alternative strategies, such as selective sampling and traditional methods of assessing within and between-class variations.

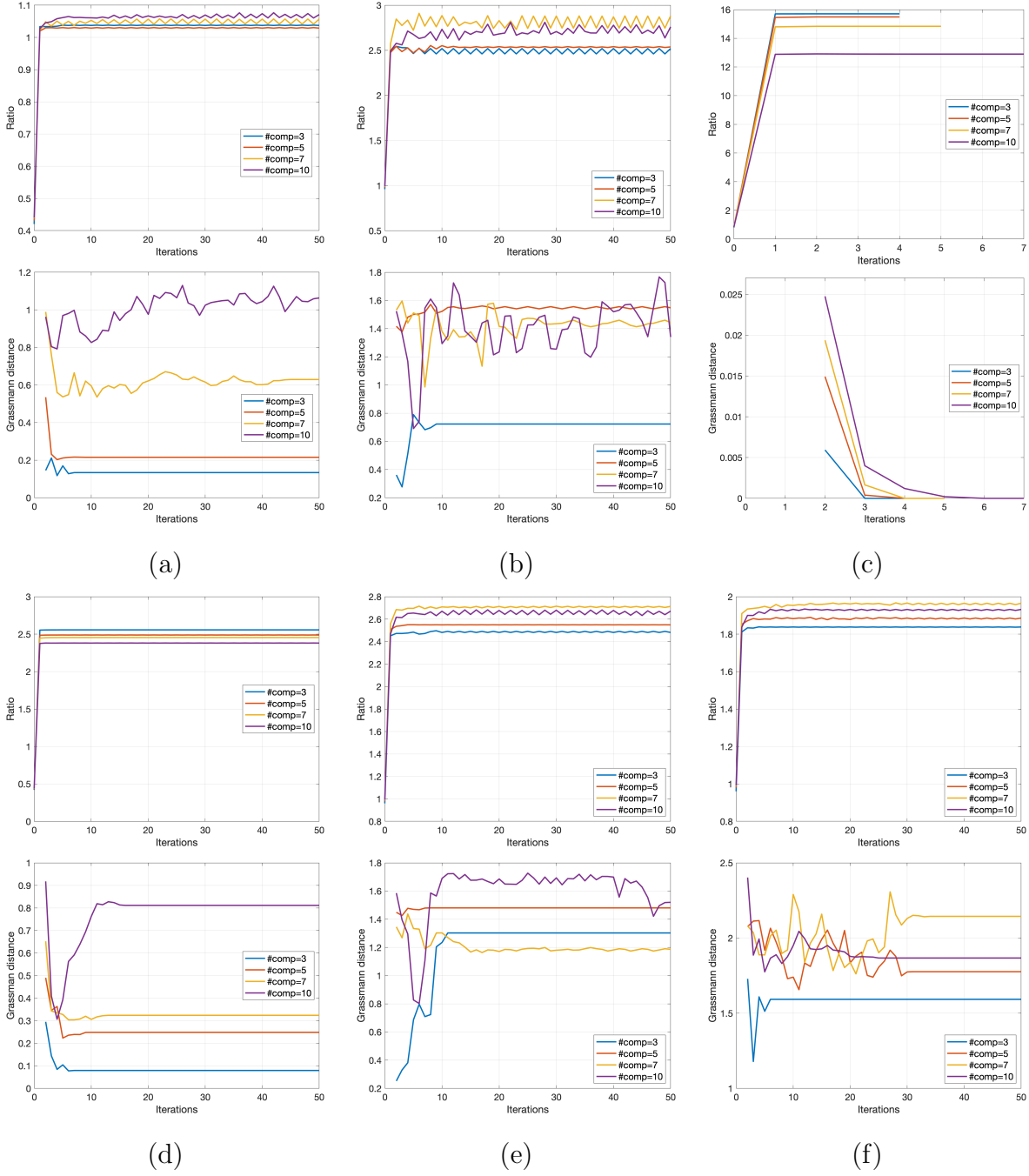


Figure 5: Convergence study based on BC, UM, and PF datasets. For each dataset, the Fisher's ratio of variations and the Grassmann distance between subspaces found in consecutive iterations are shown with respect to the number of iterations. (a)~(c): Orthonormal projection for datasets BC ($d = 40$), UM ($d = 13$), PF ($d = 1$) respectively. (d)~(f): Non-orthonormal project for BC ($d = 40$), UM ($d = 13$), and UM ($d = 25$). Here, d denotes The number of canonical variates.

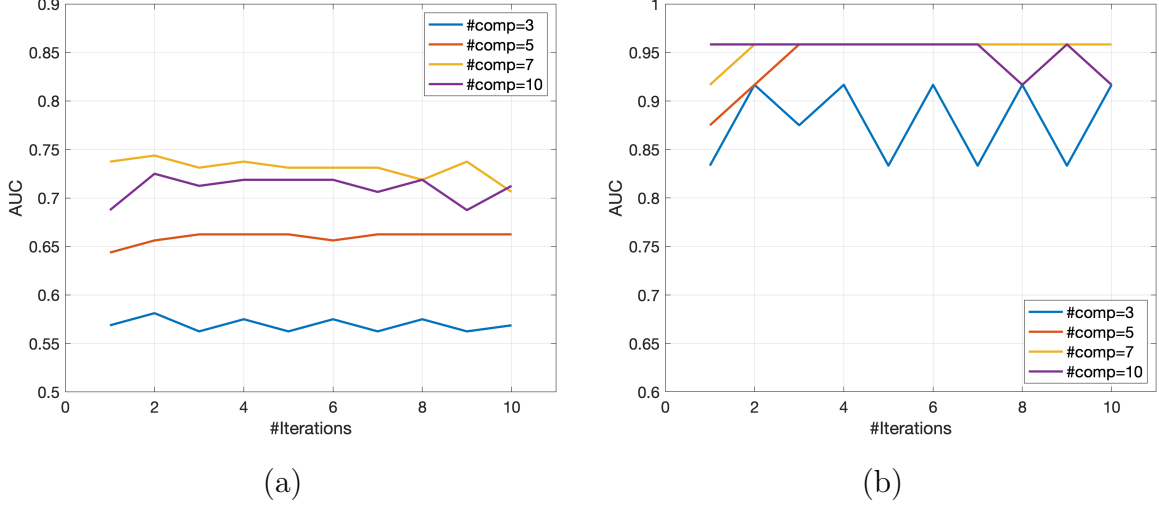


Figure 6: AUC versus the number of iterations. (a) Breast cancer data. (b) Un_melanoma data.

One such approach involves calculating the Wasserstein barycenters for each class and then evaluating variation based on the cumulative distances between individual instances and their respective class barycenters. Pursuing these methodologies could lead to the development of diverse algorithms, an area we aim to explore in future research.

A Proof for Lemma 1

We prove for the case of V_B as the proof for V_W follows likewise. Recall that

$$\bar{V}_B(A, \Pi^*) = \frac{1}{|\mathcal{I}_B|} \sum_{(k_1, k_2) \in \mathcal{I}_B} \sum_{i=1}^{m_{k_1}} \sum_{j=1}^{m_{k_2}} \pi_{i,j}^{(k_1, k_2)} \cdot \left\| A^t \cdot x_i^{(k_1)} - A^t \cdot x_j^{(k_2)} \right\|^2$$

Note that

$$\begin{aligned} & \left\| A^t \cdot x_i^{(k_1)} - A^t \cdot x_j^{(k_2)} \right\|^2 \\ &= \text{tr} \left[(A^t \cdot x_i^{(k_1)} - A^t \cdot x_j^{(k_2)})^t \cdot (A^t \cdot x_i^{(k_1)} - A^t \cdot x_j^{(k_2)}) \right] \\ &= \text{tr} \left[(A^t \cdot x_i^{(k_1)} - A^t \cdot x_j^{(k_2)}) \cdot (A^t \cdot x_i^{(k_1)} - A^t \cdot x_j^{(k_2)})^t \right] \\ &= \text{tr} \left[A^t (x_i^{(k_1)} - x_j^{(k_2)}) (x_i^{(k_1)} - x_j^{(k_2)})^t \cdot A \right]. \end{aligned}$$

Hence

$$\begin{aligned}
& \sum_{(k_1, k_2) \in \mathcal{I}_B} \sum_{i=1}^{m_{k_1}} \sum_{j=1}^{m_{k_2}} \pi_{i,j}^{(k_1, k_2)} \cdot \left\| A^t \cdot x_i^{(k_1)} - A^t \cdot x_j^{(k_2)} \right\|^2 \\
&= \sum_{(k_1, k_2) \in \mathcal{I}_B} \sum_{i=1}^{m_{k_1}} \sum_{j=1}^{m_{k_2}} \text{tr} \left[A^t \cdot \pi_{i,j}^{(k_1, k_2)} \cdot (x_i^{(k_1)} - x_j^{(k_2)})(x_i^{(k_1)} - x_j^{(k_2)})^t \cdot A \right] \\
&= \text{tr} \left[A^t \cdot \left(\sum_{(k_1, k_2) \in \mathcal{I}_B} \sum_{i=1}^{m_{k_1}} \sum_{j=1}^{m_{k_2}} \pi_{i,j}^{(k_1, k_2)} \cdot (x_i^{(k_1)} - x_j^{(k_2)})(x_i^{(k_1)} - x_j^{(k_2)})^t \right) \cdot A \right].
\end{aligned}$$

Since

$$C_B = \frac{1}{|\mathcal{I}_B|} \cdot \sum_{(k_1, k_2) \in \mathcal{I}_B} \sum_{i=1}^{m_{k_1}} \sum_{j=1}^{m_{k_2}} \pi_{i,j}^{(k_1, k_2)} \cdot (x_i^{(k_1)} - x_j^{(k_2)})(x_i^{(k_1)} - x_j^{(k_2)})^t,$$

we have shown that $\bar{V}_B(A, \Pi^*) = \text{tr}(A^t C_B A)$. The proof for $\bar{V}_W(A, \Pi^*) = \text{tr}(A^t C_W A)$ is similar and skipped here.

B Proof for Lemma 2

Recall that $\hat{\pi}$ is the joint distribution of independent random vectors Z_1 and Z_2 in \mathbb{R}^d with marginal distributions $\phi_1 \sim N(\mu_1, \Sigma_1)$ and $\phi_2 \sim N(\mu_2, \Sigma_2)$.

$$\begin{aligned}
& \widehat{W}^2(\phi_1, \phi_2) = E_{\hat{\pi}} \|Z_1 - Z_2\|^2 \\
&= E(Z_1 - Z_2)^t (Z_1 - Z_2) \\
&= E[Z_1 - \mu_1 - (Z_2 - \mu_2) + \mu_1 - \mu_2]^t [Z_1 - \mu_1 - (Z_2 - \mu_2) + \mu_1 - \mu_2] \\
&= E(Z_1 - \mu_1)^t (Z_1 - \mu_1) + E(Z_2 - \mu_2)^t (Z_2 - \mu_2) \\
&\quad - 2E(Z_1 - \mu_1)(Z_2 - \mu_2) + \|\mu_1 - \mu_2\|^2 \\
&= E(Z_1 - \mu_1)^t (Z_1 - \mu_1) + E(Z_2 - \mu_2)^t (Z_2 - \mu_2) + \|\mu_1 - \mu_2\|^2.
\end{aligned}$$

The last equality follows from the independence of Z_1 and Z_2 . Also note that

$$(Z_1 - \mu_1)^t (Z_1 - \mu_1) = \text{tr}[(Z_1 - \mu_1)^t (Z_1 - \mu_1)] = \text{tr}[(Z_1 - \mu_1)(Z_1 - \mu_1)^t]$$

Hence

$$\begin{aligned}
E(Z_1 - \mu_1)^t (Z_1 - \mu_1) &= E[\text{tr}((Z_1 - \mu_1)(Z_1 - \mu_1)^t)] \\
&= \text{tr}[E((Z_1 - \mu_1)(Z_1 - \mu_1)^t)] = \text{tr}(\Sigma_1).
\end{aligned}$$

Similarly, we have $E(Z_2 - \mu_2)^t(Z_2 - \mu_2) = \text{tr}(\Sigma_2)$. We thus have shown that

$$\widehat{W}^2(\phi_1, \phi_2) = \|\mu_1 - \mu_2\|^2 + \text{tr}[\Sigma_1 + \Sigma_2].$$

Since $\|\mu_1 - \mu_2\|^2 = \text{tr}((\mu_1 - \mu_2) \cdot (\mu_1 - \mu_2)^t)$, we also have

$$\widehat{W}^2(\phi_1, \phi_2) = \text{tr}[\Sigma_1 + \Sigma_2 + (\mu_1 - \mu_2) \cdot (\mu_1 - \mu_2)^t].$$

Since $P(\phi_i, A) \sim N(A^t \mu_i, A^t \Sigma_i A)$, $i = 1, 2$,

$$\begin{aligned} \widehat{W}^2(P(\phi_1, A), P(\phi_2, A)) &= \text{tr}[A^t \Sigma_1 A + A^t \Sigma_2 A + A^t (\mu_1 - \mu_2) \cdot (\mu_1 - \mu_2)^t A] \\ &= \text{tr}[A^t \cdot (\Sigma_1 + \Sigma_2 + (\mu_1 - \mu_2) \cdot (\mu_1 - \mu_2)^t) \cdot A]. \end{aligned}$$

C Proof for Lemma 3

We prove for the case of $\widehat{V}_B(A, \Pi^*)$. The proof for $\widehat{V}_W(A, \Pi^*)$ is similar and skipped. By Lemma 2,

$$\widehat{W}^2(P(\phi_1, A), P(\phi_2, A)) = \text{tr}[A^t \cdot (\Sigma_1 + \Sigma_2 + (\mu_1 - \mu_2) \cdot (\mu_1 - \mu_2)^t) \cdot A]. \quad (15)$$

Substitute Eq. (15) in the following:

$$\widehat{V}_B(A, \Pi^*) = \frac{1}{|\mathcal{I}_B|} \sum_{(k_1, k_2) \in \mathcal{I}_B} \sum_{i=1}^{m_{k_1}} \sum_{j=1}^{m_{k_2}} \pi_{i,j}^{(k_1, k_2)} \cdot \widehat{W}^2(P(\phi_i^{(k_1)}, A), P(\phi_j^{(k_2)}, A))$$

and apply the additive property of trace, we get

$$\widehat{V}_B(A, \Pi^*) = \text{tr}[A^t \hat{C}_B A],$$

where

$$\hat{C}_B = \frac{1}{|\mathcal{I}_B|} \sum_{(k_1, k_2) \in \mathcal{I}_B} \sum_{i=1}^{m_{k_1}} \sum_{j=1}^{m_{k_2}} \pi_{i,j}^{(k_1, k_2)} \cdot \left[\Sigma_i^{(k_1)} + \Sigma_j^{(k_2)} + (\mu_i^{(k_1)} - \mu_j^{(k_2)}) \cdot (\mu_i^{(k_1)} - \mu_j^{(k_2)})^t \right].$$

Note that

$$\sum_{i=1}^{m_{k_1}} \sum_{j=1}^{m_{k_2}} \pi_{i,j}^{(k_1, k_2)} \cdot \Sigma_i^{(k_1)} = \sum_{i=1}^{m_{k_1}} \Sigma_i^{(k_1)} \sum_{j=1}^{m_{k_2}} \pi_{i,j}^{(k_1, k_2)} = \sum_{i=1}^{m_{k_1}} p_i^{(k_1)} \Sigma_i^{(k_1)},$$

and, similarly, $\sum_{i=1}^{m_{k_1}} \sum_{j=1}^{m_{k_2}} \pi_{i,j}^{(k_1,k_2)} \cdot \Sigma_j^{(k_2)} = \sum_{j=1}^{m_{k_2}} p_j^{(k_2)} \Sigma_j^{(k_2)}$. Thus we have shown Eq. (10):

$$\begin{aligned} \hat{C}_B &= \frac{1}{|\mathcal{I}_B|} \sum_{(k_1,k_2) \in \mathcal{I}_B} \sum_{i=1}^{m_{k_1}} \sum_{j=1}^{m_{k_2}} \pi_{i,j}^{(k_1,k_2)} (\mu_i^{(k_1)} - \mu_j^{(k_2)}) \cdot (\mu_i^{(k_1)} - \mu_j^{(k_2)})^t \\ &\quad + \frac{1}{|\mathcal{I}_B|} \sum_{(k_1,k_2) \in \mathcal{I}_B} \left[\sum_{i=1}^{m_{k_1}} p_i^{(k_1)} \Sigma_i^{(k_1)} + \sum_{j=1}^{m_{k_2}} p_j^{(k_2)} \Sigma_j^{(k_2)} \right]. \end{aligned}$$

D Proof for Theorem 1

Suppose at iteration τ , we have obtained direction a^τ . Let $\pi^{(k_1,k_2),\tau}$ be the optimal couplings between $P(Q_{k_1}, a^\tau)$ and $P(Q_{k_2}, a^\tau)$, $(k_1, k_2) \in \mathcal{I}_B \cup \mathcal{I}_W$. Again denote the collection of optimal couplings at the τ th iteration by Π^τ . Then

$$r(a^\tau) = \frac{\bar{V}_B(a^\tau)}{\bar{V}_W(a^\tau)} = \frac{\bar{V}_B(a^\tau, \Pi^\tau)}{\bar{V}_W(a^\tau, \Pi^\tau)}.$$

In the step of updating $a^{\tau+1}$, by Lemma 1 for the case of discrete distributions and Lemma 3 for the case of GMMs, OTAF solves

$$r(a^{\tau+1}, \Pi^\tau) = \max_{a \in \mathbb{R}^d} r(a, \Pi^\tau) = \frac{\bar{V}_B(a, \Pi^\tau)}{\bar{V}_W(a, \Pi^\tau)}.$$

We thus have $r(a^{\tau+1}, \Pi^\tau) \geq r(a^\tau)$. If we assume that $r(a^{\tau+1}, \Pi^{\tau+1}) \geq r(a^{\tau+1}, \Pi^\tau)$, we get $r(a^{\tau+1}) = r(a^{\tau+1}, \Pi^{\tau+1}) \geq r(a^\tau)$.

References

Aleman, A., Upadhyaya, B., Tuballes, K., Kappes, K., Gleason, C., Beach, K., Agte, S., Srivastava, K., Andre, D., Azad, A., Banu, R., Bermúdez-González, M. C., Cai, G., Cognigni, C., David, K., Floda, D., Firpo, A., Kleiner, G., Lyttle, N., Mendez, W., Mulder, L. C. F., Mendu, R., Oostenink, A., Rooker, A., Russo, K., Salimbangon, A., Saksena, M., Shin, A., Sominsky, L., Van Oekelen, O., Barcessat, V., Bhardwaj, N., Kim-Schulze, S., Gnjjatic, S., Brown, B., Cordon-Cardo, C., Krammer, F., Merad, M., Jagannath, S., Wajnberg, A., Simon, V., and Parekh, S. (2021). Variable cellular

- responses to SARS-CoV-2 in fully vaccinated patients with multiple myeloma. *Cancer Cell*, 39(11):1442–1444.
- Benamou, J.-D., Carlier, G., Cuturi, M., Nenna, L., and Peyré, G. (2015). Iterative Bregman projections for regularized transportation problems. *SIAM J. Sci. Comp. (SJSC)*, 37(2):A1111–A1138.
- Bonneel, N., Rabin, J., Peyré, G., and Pfister, H. (2015). Sliced and radon wasserstein barycenters of measures. *Journal of Mathematical Imaging and Vision*, 51:22–45.
- Brummelman, J., Haftmann, C., Núñez, N. G., Alvisi, G., Mazza, E. M. C., Becher, B., and Lugli, E. (2019). Development, application and computational analysis of high-dimensional fluorescent antibody panels for single-cell flow cytometry. *Nature Protocols*, 14(7):1946–1969.
- Chen, Y., Ye, J., and Li, J. (2019). Aggregated Wasserstein distance and state registration for hidden Markov models. *IEEE transactions on pattern analysis and machine intelligence*, 42(9):2133–2147.
- Cuturi, M. (2013). Sinkhorn distances: Lightspeed computation of optimal transport. In Burges, C., Bottou, L., Welling, M., Ghahramani, Z., and Weinberger, K., editors, *Advances in Neural Information Processing Systems*, volume 26. Curran Associates, Inc.
- Delon, J. and Desolneux, A. (2020). A Wasserstein-type distance in the space of Gaussian mixture models. *SIAM Journal on Imaging Sciences*, 13(2):936–970.
- Deshpande, I., Hu, Y.-T., Sun, R., Pyrros, A., Siddiqui, N., Koyejo, S., Zhao, Z., Forsyth, D., and Schwing, A. G. (2019). Max-sliced wasserstein distance and its use for gans. In *Proceedings of the IEEE/CVF conference on computer vision and pattern recognition*, pages 10648–10656.
- Durante, M. A., Rodriguez, D. A., Kurtenbach, S., Kuznetsov, J. N., Sanchez, M. I., Decatur, C. L., Snyder, H., Feun, L. G., Livingstone, A. S., and Harbour, J. W. (2020). Single-cell analysis reveals new evolutionary complexity in uveal melanoma. *Nature Communications*, 11(1):496.

- Flamary, R., Cuturi, M., Courty, N., and Rakotomamonjy, A. (2018). Wasserstein discriminant analysis. *Machine Learning*, 107:1923–1945.
- Furman, D., Jovic, V., Kidd, B., Shen-Orr, S., Price, J., Jarrell, J., Tse, T., Huang, H., Lund, P., Maecker, H. T., Utz, P. J., Dekker, C. L., Koller, D., and Davis, M. M. (2013). Apoptosis and other immune biomarkers predict influenza vaccine responsiveness. *Molecular Systems Biology*, 9(1):659.
- Habermann, A. C., Gutierrez, A. J., Bui, L. T., Yahn, S. L., Winters, N. I., Calvi, C. L., Peter, L., Chung, M.-I., Taylor, C. J., Jetter, C., Raju, L., Roberson, J., Ding, G., Wood, L., Sucre, J. M. S., Richmond, B. W., Serezani, A. P., McDonnell, W. J., Mallal, S. B., Bacchetta, M. J., Loyd, J. E., Shaver, C. M., Ware, L. B., Bremner, R., Walia, R., Blackwell, T. S., Banovich, N. E., and Kropski, J. A. (2020). Single-cell RNA sequencing reveals profibrotic roles of distinct epithelial and mesenchymal lineages in pulmonary fibrosis. *Science Advances*, 6(28):eaba1972.
- Hastie, T., Tibshirani, R., Friedman, J. H., and Friedman, J. H. (2009). *The elements of statistical learning: data mining, inference, and prediction*, volume 2. Springer.
- Kolouri, S., Nadjahi, K., Simsekli, U., Badeau, R., and Rohde, G. (2019). Generalized sliced wasserstein distances. *Advances in neural information processing systems*, 32.
- Korthauer, K. D., Chu, L.-F., Newton, M. A., Li, Y., Thomson, J., Stewart, R., and Kendziora, C. (2016). A statistical approach for identifying differential distributions in single-cell RNA-seq experiments. *Genome Biology*, 17(1):222.
- Lin, L., Finak, G., Ushey, K., Seshadri, C., Hawn, T. R., Frahm, N., Scriba, T. J., Mahomed, H., Hanekom, W., Bart, P.-A., Pantaleo, G., Tomaras, G. D., Rerks-Ngarm, S., Kaewkungwal, J., Nitayaphan, S., Pitisuttithum, P., Michael, N. L., Kim, J. H., Robb, M. L., O’Connell, R. J., Karasavvas, N., Gilbert, P., C De Rosa, S., McElrath, M. J., and Gottardo, R. (2015). COMPASS identifies T-cell subsets correlated with clinical outcomes. *Nature Biotechnology*, 33(6):610–616.

- Lin, L., Shi, W., Ye, J., and Li, J. (2023). Multisource single-cell data integration by MAW barycenter for Gaussian mixture models. *Biometrics*, 79(2):866–877.
- Lingblom, C. M. D., Kowli, S., Swaminathan, N., Maecker, H. T., and Lambert, S. L. (2018). Baseline immune profile by CyTOF can predict response to an investigational adjuvanted vaccine in elderly adults. *Journal of Translational Medicine*, 16(1):153.
- Paty, F.-P. and Cuturi, M. (2019). Subspace robust wasserstein distances. In *International conference on machine learning*, pages 5072–5081. PMLR.
- Pele, O. and Werman, M. (2009). Fast and robust Earth Mover’s Distances. In *2009 IEEE 12th International Conference on Computer Vision*, pages 460–467.
- Qiao, M. and Li, J. (2016). Distance-based mixture modeling for classification via hypothetical local mapping. *Statistical Analysis and Data Mining: The ASA Data Science Journal*, 9(1):43–57.
- Rubio, A. M., Everaert, C., Damme, E. V., Preter, K. D., and Vermaelen, K. (2023). Circulating immune cell dynamics as outcome predictors for immunotherapy in non-small cell lung cancer. *Journal for ImmunoTherapy of Cancer*, 11(8).
- Stefanski, A.-L., Rincon-Arevalo, H., Schrezenmeier, E., Karberg, K., Szelinski, F., Ritter, J., Chen, Y., Jahrsdörfer, B., Ludwig, C., Schrezenmeier, H., Lino, A. C., and Dörner, T. (2022). B cell characteristics at baseline predict vaccination response in RTX treated patients. *Frontiers in Immunology*, 13.
- Villani, C. (2003). *Topics in Optimal Transportation*. American Mathematical Soc.
- Wang, J., Wang, P., and Shafto, P. (2023). Efficient discretization of optimal transport. *Entropy*, 25(6).
- Wu, S. Z., Al-Eryani, G., Roden, D. L., Junankar, S., Harvey, K., Andersson, A., Thennavan, A., Wang, C., Torpy, J. R., Bartonicek, N., Wang, T., Larsson, L., Kaczorowski, D., Weisenfeld, N. I., Uytingco, C. R., Chew, J. G., Bent, Z. W., Chan, C.-L., Gnanasambandapillai, V., Dutertre, C.-A., Gluch, L., Hui, M. N., Beith, J., Parker, A., Robbins,

- E., Segara, D., Cooper, C., Mak, C., Chan, B., Warriar, S., Ginhoux, F., Millar, E., Powell, J. E., Williams, S. R., Liu, X. S., O’Toole, S., Lim, E., Lundeberg, J., Perou, C. M., and Swarbrick, A. (2021). A single-cell and spatially resolved atlas of human breast cancers. *Nature Genetics*, 53(9):1334–1347.
- Yang, L., Li, J., Sun, D., and Toh, K.-C. (2021). A fast globally linearly convergent algorithm for the computation of wasserstein barycenters. *Journal of Machine Learning Research*, 22(21):1–37.
- Ye, J., Wu, P., Wang, J. Z., and Li, J. (2017). Fast discrete distribution clustering using wasserstein barycenter with sparse support. *IEEE Transactions on Signal Processing*, 65(9):2317–2332.
- Ye, K. and Lim, L.-H. (2016). Schubert varieties and distances between subspaces of different dimensions. *SIAM Journal on Matrix Analysis and Applications*, 37(3):1176–1197.
- Zhang, J., Li, J., and Lin, L. (2023). Statistical and machine learning methods for immunoprofiling based on single-cell data. *Human Vaccines & Immunotherapeutics*, page 2234792.
- Zhang, M. and Guo, F. R. (2022). BSDE: barycenter single-cell differential expression for case–control studies. *Bioinformatics*, 38(10):2765–2772.
- Zhang, M., Liu, S., Miao, Z., Han, F., Gottardo, R., and Sun, W. (2022). IDEAS: individual level differential expression analysis for single-cell RNA-seq data. *Genome Biology*, 23(1):33.